GEOPHYSICS, VOL. 73, NO. 2 (MARCH-APRIL 2008); P. S47–S61, 12 FIGS.
10.1190/1.2838043

Interferometric imaging condition for wave-equation migration

Paul Sava[1] and Oleg Poliannikov[2]

ABSTRACT

The fidelity of depth seismic imaging depends on the accuracy of the velocity models used for wavefield reconstruction. Models can be decomposed in two components, corresponding to large-scale and small-scale variations. In practice, the large-scale velocity model component can be estimated with high accuracy using repeated migration/tomography cycles, but the small-scale component cannot. When the earth has significant small-scale velocity components, wavefield reconstruction does not completely describe the recorded data, and migrated images are perturbed by artifacts. There are two possible ways to address this problem: (1) improve wavefield reconstruction by estimating more accurate velocity models and image using conventional techniques (e.g., wavefield crosscorrelation) or (2) reconstruct wavefields with conventional methods using the known background velocity model but improve the imaging condition to alleviate the artifacts caused by the imprecise reconstruction. We describe the unknown component of the velocity model as a random function with local spatial correlations. Imaging data perturbed by such random variations is characterized by statistical instability, i.e., various wavefield components image at wrong locations that depend on the actual realization of the random model. Statistical stability can be achieved by preprocessing the reconstructed wavefields prior to the imaging condition. We use Wigner distribution functions to attenuate the random noise present in the reconstructed wavefields, parameterized as a function of image coordinates. Wavefield filtering using Wigner distribution functions and conventional imaging can be lumped together into a new form of imaging condition that we call an interferometric imaging condition because of its similarity to concepts from recent work on interferometry. The interferometric imaging condition can be formulated both for zero-offset and for multioffset data, leading to robust, efficient imaging procedures that effectively attenuate imaging artifacts caused by unknown velocity models.

INTRODUCTION

Seismic imaging in complex media requires accurate knowledge of the medium's velocity. Assuming single scattering (Born approximation), imaging requires propagation of the recorded wavefields from the acquisition surface, followed by the application of an imaging condition highlighting locations where backscattering occurs, i.e., where reflectors are present. Typically, this is achieved with simple image-processing techniques, e.g., crosscorrelation of wavefields reconstructed from sources and receivers.

The main requirement for good-quality imaging is accurate knowledge of the velocity model. Errors in the model used for imaging lead to inaccurate reconstruction of the seismic wavefields and to distortions of the migrated images. In any realistic seismic field experiment, the velocity model is never known exactly. Migration-velocity analysis estimates large-scale approximations of the model, but some fine-scale variations always remain elusive. For example, when geology includes complicated stratigraphic structures or complex salt/carbonate bodies, the rapid velocity variations on the scale of the seismic wavelength and smaller cannot be estimated correctly by kinematic methods. Therefore, even if the broad kinematics of the

Manuscript received by the Editor 27 December 2006; revised manuscript received 31 October 2007; published online 4 March 2008.
[1]Colorado School of Mines, Department of Geophysics, Golden, Colorado, U.S.A. E-mail: psava@mines.edu.
[2]Massachusetts Institute of Technology, Earth Resources Laboratory, Cambridge, Massachusetts, U.S.A. E-mail: poliann@erl.mit.edu.
© 2008 Society of Exploration Geophysicists. All rights reserved.

seismic wavefields are reconstructed correctly, the extrapolated wavefields also contain phase and amplitude distortions that lead to image artifacts, obstructing the image of the geologic structure under consideration.

Although, it is certainly true that even the recovery of a long-wave background may prove to be a challenge in some circumstances, we do not attempt to address that issue in this paper. Instead, we concentrate on the problem of dealing with the effect of small-scale random variations not estimated by conventional methods.

We can approach this problem in two ways. The first option is to improve our velocity-analysis methods to estimate the small-scale variations in the model. Such techniques take advantage of all information contained in seismic wavefields and are not limited to kinematic information of selected events picked from the data. Examples of techniques in this category are waveform inversion (Tarantola, 1987; Pratt, 1990; Pratt and Worthington, 1990; Sirgue and Pratt, 2004), wave-equation tomography (Woodward, 1992), and wave-equation migration velocity analysis (Sava and Biondi, 2004a, b; Shen et al., 2005). A more accurate velocity model allows for more accurate wavefield reconstruction. Then, wavefields can be used for imaging using conventional procedures, e.g., crosscorrelation.

The second option is to concentrate on the imaging condition rather than concentrate on perfect wavefield reconstruction. Assuming that the large-scale component of the velocity models is known (e.g., by iterative migration/tomography cycles), we can design imaging conditions that are not sensitive to small inaccuracies of the reconstructed wavefields. Imaging artifacts can be reduced at the imaging condition step, despite the fact that the wavefields incorporate small kinematic errors caused by velocity fluctuations.

Of course, the two options complement each other, and both can contribute to imaging accuracy. In this article, we concentrate on the second approach. For purposes of theoretical analysis, it is convenient to model the small-scale velocity fluctuations as random but spatially correlated variations superimposed on a known velocity. We assume that we know the background model but that we do not know the random fluctuations. The goal is to design an imaging condition that alleviates artifacts caused by those random fluctuations. Conventional imaging consists of crosscorrelations of extrapolated source and receiver wavefields at image locations. Wavefield extrapolation uses an approximation of the true model, so the wavefields contain random time delays, or equivalently random phases, that lead to imaging artifacts.

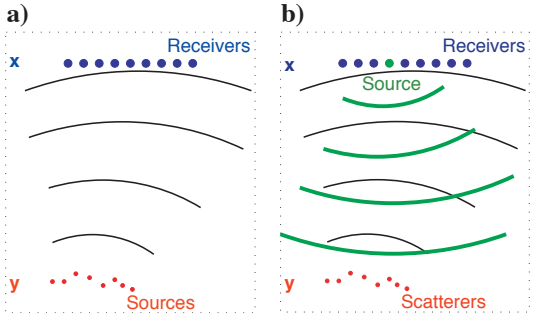


Figure 1. (a) Zero-offset seismic experiment sketch and (b) multioffset seismic experiment sketch. Coordinates $\mathbf{x} = \{x, y\}$ characterize receiver positions on the surface, and coordinates $\mathbf{y} = \{x, y, z\}$ characterize reflector positions in the subsurface.

One way of mitigating the effects of the random model on the quality of the resulting image is to use techniques based on acoustic time reversal (Fink, 1999). Under certain assumptions, a signal sent through a random medium, recorded by a receiver array, time reversed, and sent back through the same medium, refocuses at the source location in a statistically stable fashion. Statistical stability means that the refocusing properties (i.e., image quality) are independent of the actual realization of the random medium (Papanicolaou et al., 2004; Fouque et al., 2005).

We investigate an alternative way of increasing imaging statistical stability. Instead of imaging the reconstructed wavefields directly, we first apply a transformation based on Wigner distribution functions (WDFs; Wigner, 1932) to the reconstructed wavefields. We consider a special case of WDF that attenuates random fluctuations from the wavefields after extrapolation with conventional techniques. The idea for this method is borrowed from image processing, where WDFs are used for filtering random noise. Here, we apply WDFs to the reconstructed wavefields, prior to the imaging condition. This is in contrast to data filtering prior to wavefield reconstruction or to image filtering after applying an imaging condition.

Our procedure closely resembles conventional imaging procedures, wherein wavefields are extrapolated in the image volume and then crosscorrelated in time at every image location. We use WDFs defined in 3D windows around image locations, which makes the method both robust and efficient. From an implementation and computational cost point of view, our technique is similar to conventional imaging, but its statistical properties are better. Although conceptually separate, we can lump together the WDF transformation and conventional imaging into a new form of imaging condition that resembles interferometric techniques. Therefore, we use the name interferometric imaging condition for our technique to contrast it with the conventional imaging condition.

A related method discussed in the literature is coherent interferometric imaging (Borcea et al., 2006a, b, c). This method uses similar local crosscorrelations and averaging, but unlike our method, it parameterizes reconstructed wavefields as a function of receiver coordinates. Thus, the coherent interferometric-imaging functional requires separate wavefield reconstruction from every receiver position, which makes the technique prohibitively expensive and probably unusable in practice on large-scale seismic-imaging projects. In contrast, the imaging technique advocated in this paper achieves similar statistical stability properties as coherent interferometric imaging but at an affordable cost because we apply wavefield reconstruction only once for all receiver locations corresponding to a given seismic experiment, typically a "shot."

IMAGING CONDITIONS

Conventional imaging condition

Let $D(\mathbf{x},t)$ be the data recorded at time t at receivers located at coordinates $\mathbf{x}$ for a seismic experiment with buried sources (Figure 1a) also known as an exploding-reflector seismic experiment

(Loewenthal et al., 1976). A conventional imaging procedure for this type of data consists of two steps (Claerbout, 1985): wavefield reconstruction at image coordinates **y** from data recorded at receiver coordinates **x**, followed by an imaging condition taking the reconstructed wavefield at time $t = 0$ as the seismic image.

Mathematically, we can represent the wavefield V reconstructed at coordinates **y** from data D recorded at **x** as a temporal convolution of the recorded trace, with the Green's function G connecting the two points:

$$V(\mathbf{x},\mathbf{y},t) = D(\mathbf{x},t) *_t G(\mathbf{x},\mathbf{y},t). \quad (1)$$

The total wavefield U reconstructed at **y** from all receivers is the superposition of the wavefields V reconstructed from individual traces:

$$U(\mathbf{y},t) = \int_{\mathbf{x}} d\mathbf{x} V(\mathbf{x},\mathbf{y},t), \quad (2)$$

where the integral over **x** spans the entire receiver space. As stated, the imaging condition extracts the image $R(\mathbf{y})$ from the wavefield $U(\mathbf{y},t)$ at time $t = 0$, i.e.,

$$R(\mathbf{y}) = U(\mathbf{y},t=0). \quad (3)$$

The Green's function used in the procedure described by equation 1 can be implemented in different ways. For our purposes, the actual method used to compute the Green's functions is irrelevant. Any procedure can be used, although different procedures will be appropriate in different situations, with different costs of implementation. We assume that a satisfactory procedure exists and is appropriate for the respective velocity models used for the simulations. In our examples, we compute the Green's functions with time-domain, finite-difference solutions to the acoustic-wave equation, similar to reverse-time migration (Baysal et al., 1983).

Consider the velocity model depicted in Figure 2a and the imaging target depicted in Figure 2b. We assume that the model with random fluctuations (Figure 3b) represents the real subsurface velocityand use this model to simulate data. We consider the background model (Figure 3a) to represent the migration velocity and use this model to migrate the data simulated in the random model. We consider one source located in the subsurface at coordinates $z = 8$ km and $x = 13.5$ km, and receivers located close to the top of the model at discrete horizontal positions and depth $z = 0.0762$ km. Figure 3a-d shows snapshots of the simulated wavefields at a later time. The panels on the left correspond to modeling in the background model; the panels on the right correspond to modeling in the random model.

Figure 3f shows the data recorded on the surface. The direct wavefield arrival from the seismic source is identified easily in the data, although the wavefronts are distorted by the random perturbations in the medium. For comparison, Figure 3e shows data simulated in the background model, which do not show random fluctuations.

Conventional imaging using the procedure described above implicitly states that data generated in the random model (Figure 3b) are processed as if they were generated in the background model (Figure 3a). Thus, the random-phase variations in the data are not properly compensated during imaging, causing artifacts in the image. Looking ahead, we see Figure 6b shows the image obtained by migrating data from Figure 3f using the model from Figure 3a. For comparison, Figure 6a shows the image obtained by migrating the data from Figure 3e using the same model from Figure 3a.

Ignoring aperture effects, the artifacts observed in the images are caused only because the velocity models used for modeling and migration are not the same. Small artifacts caused by truncating the data on the acquisition surface can also be observed, but those artifacts are well known (i.e., truncation butterflies) and are not the subject of our analysis. In this example, the wavefield-reconstruction procedure is the same for both modeling and migration (i.e., time-domain finite-difference solution to the acoustic-wave equation); thus, it is not causing artifacts in the image. We can conclude that the

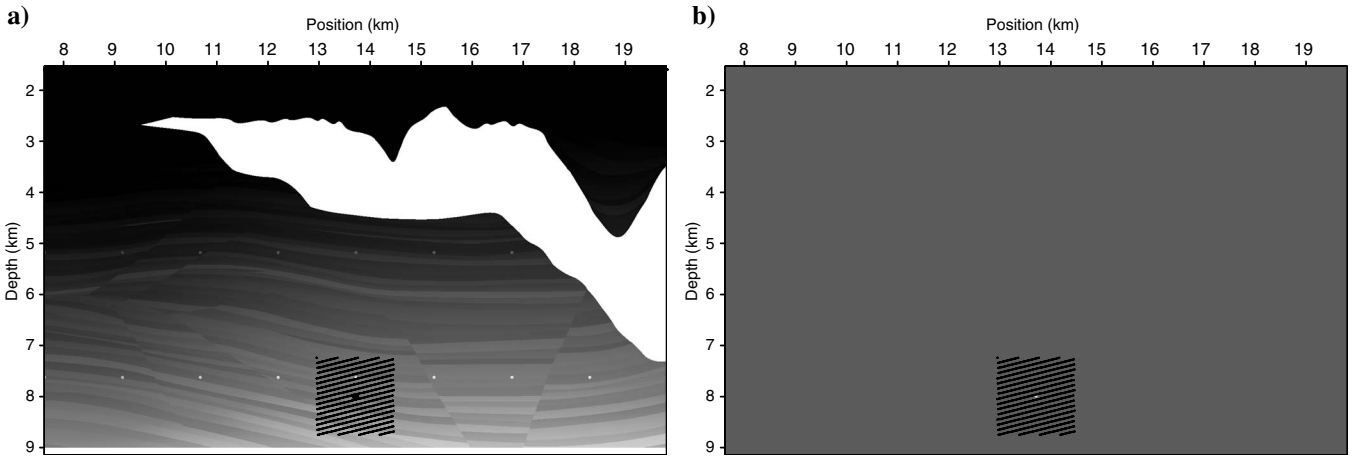


Figure 2. (a) Velocity model and (b) imaging target located around $z = 8$ km. The shaded area is imaged in Figure 6a-d.

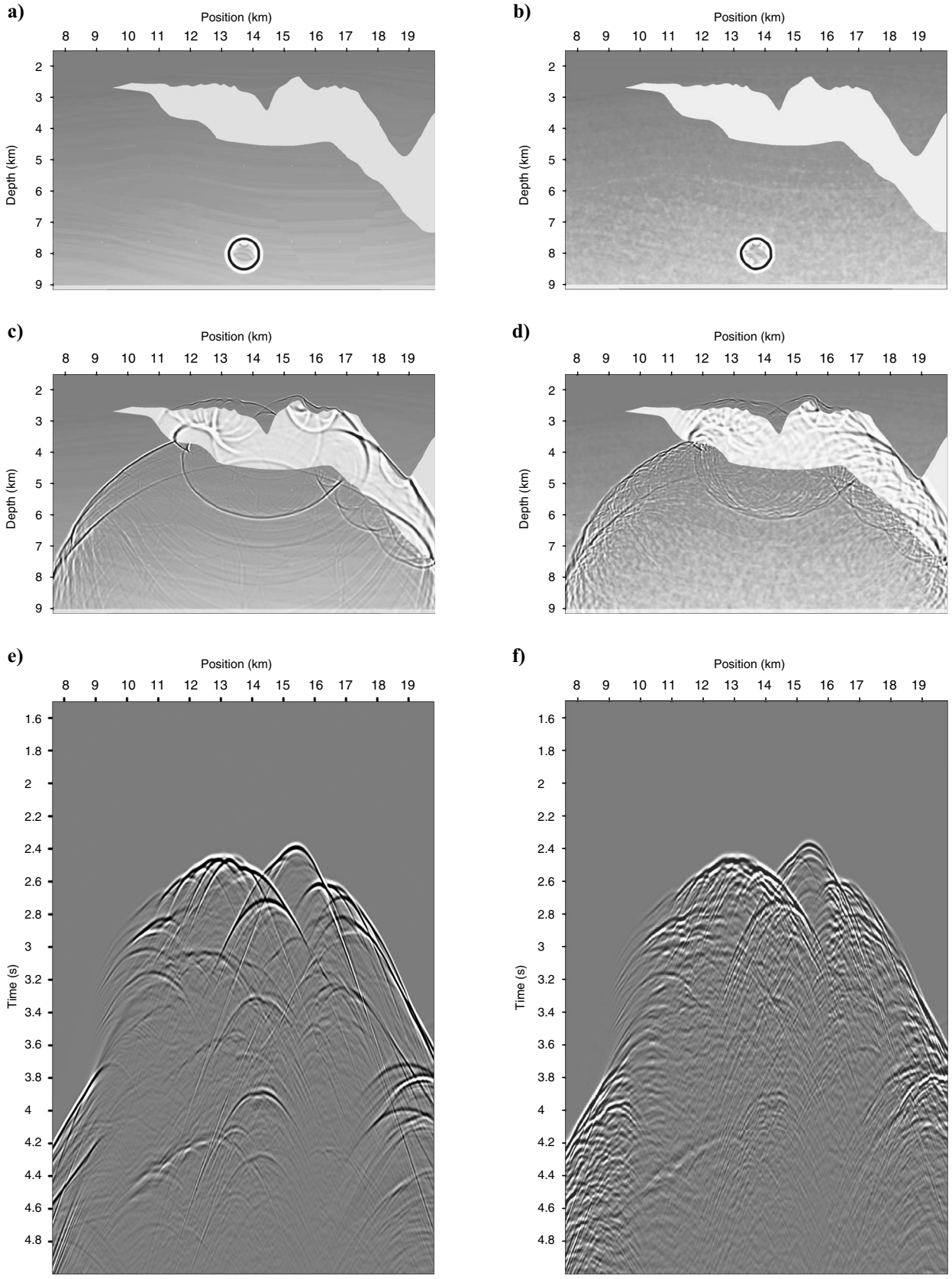


Figure 3. Seismic snapshots of acoustic wavefields simulated (a and c) in the background velocity model and (b and d) in the random velocity model. Data recorded at the surface (e) from the simulation in the background velocity model and (f) from the simulation in the random velocity model.

migration artifacts are caused by the phase differences between the Green's functions used for modeling (with the random velocity) and the Green's functions used for migration (with the background velocity). The main challenge for imaging in media with random variations is to design procedures that attenuate the random-phase delays introduced in the recorded data by the unknown variations of the medium without damaging the real reflections present in the data.

The random-phase fluctuations observed in recorded data (Figure 3f) are preserved during wavefield reconstruction using the background-velocity model. We can observe the randomness in the extrapolated wavefields in two ways: by reconstructing wavefields using individual data traces separately or by reconstructing wavefields using all data traces at once.

The first option is to reconstruct the seismic wavefield at all image locations $\mathbf{y}$ from individual receiver positions on the surface. Of course, this is not conventionally done in reverse-time imaging, but we describe this concept for illustration. Figure 4a shows the wavefield at the source position reconstructed from individual data traces depicted in Figure 3f using the background model depicted in Figure 3b. In Figure 4a, the horizontal axis corresponds to receiver positions on the surface, i.e., coordinates $\mathbf{x}$, and the vertical axis represents time.

According to our notation, Figure 4a shows the wavefield $V(\mathbf{x},\mathbf{y},t)$ reconstructed to a particular image coordinate $\mathbf{y}$ from separate traces located on the surface at coordinates $\mathbf{x}$. A similar plot can be constructed for all other image locations. Ideally, the reconstructed wavefield should line up at time $t = 0$, but this is not what we observe in this figure, indicating that the input data contain random-phase delays that are not compensated during wavefield reconstruction using the background velocity.

The second option is to reconstruct the seismic wavefield at all image locations $\mathbf{y}$ from all receiver positions on the surface at once. This is a conventional procedure for reverse-time imaging. Figure 5a shows the wavefield reconstructed from all data traces depicted in Figure 3f using the background model depicted in Figure 3b. In Figure 5a, the vertical and horizontal axes correspond to depth and horizontal positions around the source, i.e., coordinates $\mathbf{y}$, and the third cube axis represents time. According to our notation, Figure 5a corresponds to wavefield $U(\mathbf{y},t)$ reconstructed from data at all receiver coordinates $\mathbf{x}$ to image coordinates $\mathbf{y}$. The reconstructed wavefield does not focus completely at the image coordinate and time $t = 0$, indicating the input data contain random-phase delays that are not compensated during wavefield reconstruction using the background velocity.

Wigner distribution functions (WDFs)

One possible way to address the problem of random fluctuations in reconstructed wavefields is to use WDFs (Wigner, 1932) to preprocess the wavefields prior to the application of the imaging condition. Appendix A provides a brief introduction for readers unfamiliar with WDFs. More details about this topic are presented by Cohen (1995).

WDFs are bilinear representations of multidimensional signals defined in phase space, i.e., they depend simultaneously on position wavenumber ($\mathbf{y} - \mathbf{k}$) and time frequency ($t - \omega$). Wigner (1932) develops these concepts in the context of quantum physics as probability functions for the simultaneous description of coordinates and momenta of a given wave function. WDFs were introduced to signal processing by Ville (1948) and have since found many applications in signal and image processing, speech recognition, and optics.

A variation of WDFs, called pseudo-WDFs are constructed using small windows localized in space and/or time (Appendix A). Pseudo-WDFs are simple transformations with efficient application to multidimensional signals. In this paper, we apply the pseudo-WDF transformation to multidimensional seismic wavefields obtained by reconstruction from recorded seismic data. We use pseudo-WDFs for decomposition and filtering of extrapolated space-time signals as a function of their local wavenumber frequency. In particular, pseudo-WDFs can filter reconstructed wavefields to retain their coherent components by removing high-frequency noise associated with random fluctuations in the wavefields caused random fluctuations in the model.

Our method is simple: Instead of imaging the reconstructed wavefields directly, we first filter them using pseudo-WDFs to attenuate the random-phase noise and then proceed to imaging using a conventional or an extended imaging condition. Wavefield filtering occurs during the application of the zero-frequency end member of the pseudo-WDF transformation, which reduces the random character of the field. Henceforth, we use WDF to denote this special case of pseudo-WDFs, not its general form.

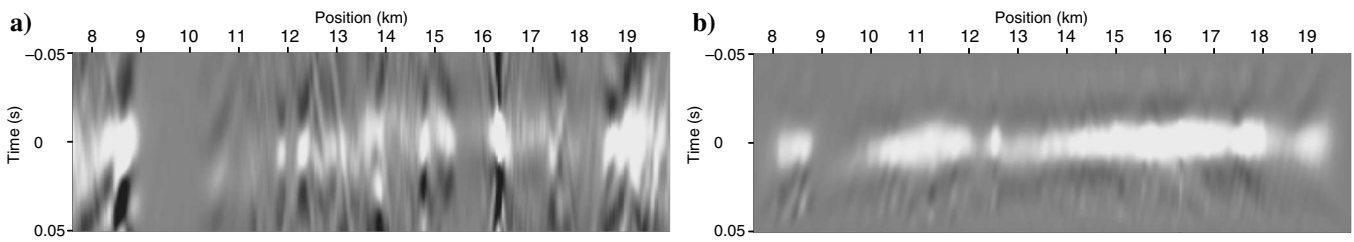


Figure 4. (a) Reconstructed seismic wavefield as a function of data coordinates and (b) its pseudo-WDF computed as a function of data coordinates $\mathbf{x}$ and time t. The wavefield is reconstructed using the background model from data simulated in the random model.

As described earlier, we can distinguish two options. The first option is to use wavefield parameterization as a function of data coordinates $\mathbf{x}$. In this case, we can write the WDF of the reconstructed wavefield $V(\mathbf{x},\mathbf{y},t)$ as

$$V_x(\mathbf{x},\mathbf{y},t) = \int_{|t_h|\le T} dt_h \int_{|\mathbf{x}_h|\le X} d\mathbf{x}_h \times V\left(\mathbf{x} - \frac{\mathbf{x}_h}{2},\mathbf{y},t - \frac{t_h}{2}\right) V\left(\mathbf{x} + \frac{\mathbf{x}_h}{2},\mathbf{y},t + \frac{t_h}{2}\right), \tag{4}$$

where $\mathbf{x}_h$ and t_h are variables spanning space and time intervals of total extent X and T, respectively. For 3D surface acquisition geometry, the 2D variable $\mathbf{x}_h$ is defined on the acquisition surface. The second option is to use wavefield parameterization as a function of image coordinates $\mathbf{y}$. In this case, we can write the WDF of the reconstructed wavefield $U(\mathbf{y},t)$ as

$$W_y(\mathbf{y},t) = \int_{|t_h|\le T} dt_h \int_{|\mathbf{y}_h|\le Y} d\mathbf{y}_h \times U\left(\mathbf{y} - \frac{\mathbf{y}_h}{2},t - \frac{t_h}{2}\right) U\left(\mathbf{y} + \frac{\mathbf{y}_h}{2},t + \frac{t_h}{2}\right), \tag{5}$$

where $\mathbf{y}_h$ and t_h are variables spanning space and time intervals of total extent Y and T, respectively. For 3D surface-acquisition geometry, the 3D variable $\mathbf{y}_h$ is defined around image positions.

For the examples used in this section, we use 41 grid points for the interval X centered around a particular receiver position, 5×5 grid points for the interval Y centered around a particular image point, and 21 grid points for the interval T centered around a particular time. These parameters are not necessarily optimal for the transformation because they characterize the local WDF windows and depend on the specific implementation of the WDF transformation. The main criterion used for selecting the size of the space-time window for the WDF transformation is avoiding crosstalk between nearby events, e.g., reflections. Finding the optimal size of this window is important for our method, although its complete treatment falls outside the scope of this article. Preliminary results on optimal window selection are discussed by Borcea et al. (2006a).

Figure 4b depicts the result of applying the WDF transformation to the reconstructed wavefield in Figure 4a. For the case of modeling in the random model and reconstruction in the background model, the pseudo-WDF attenuates the random character of the wavefield significantly (Figure 4b). The random character of the reconstructed wavefield is reduced, and the main events cluster more closely around time $t = 0$. Similarly, Figure 5b depicts the results of applying the pseudo-WDF transformation to the reconstructed wavefields in Figure 5a. For the case of modeling in the random model and reconstruction in the background model, the pseudo-WDF also attenuates the random character of the wavefield significantly (Figure 5b), and the main events focus at the correct image location at time $t = 0$.

Zero-offset interferometric imaging condition

After filtering the reconstructed wavefields with WDFs, we can perform imaging with normal procedures. For wavefields parameterized as a function of data coordinates, we obtain the total wavefield at image coordinates by summing over receiver coordinates $\mathbf{x}$:

$$W_x(\mathbf{y},t) = \int_{\mathbf{x}} d\mathbf{x} V_x(\mathbf{x},\mathbf{y},t), \tag{6}$$

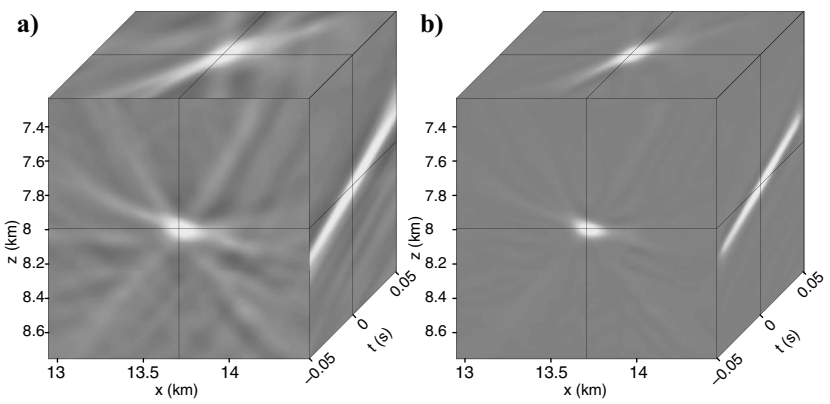


Figure 5. (a) Reconstructed seismic wavefield as a function of image coordinates and (b) its pseudo-WDF computed as a function of image coordinates $\mathbf{y}$ and time t. The wavefield is reconstructed using the background model from data modeled in the random model.

followed by a conventional imaging-condition extracting time $t = 0$ from the WDF of the reconstructed wavefields:

$$R_x(\mathbf{y}) = W_x(\mathbf{y}, t = 0). \tag{7}$$

The image obtained with this imaging procedure is shown in Figure 6c. As expected, the artifacts caused by the unknown random fluctuations in the model are reduced, leaving a cleaner image of the source.

Similarly, for wavefields parameterized as a function of image coordinates, we obtain the image by applying the conventional imaging condition, extracting time $t = 0$ from the WDF of the reconstructed wavefield:

$$R_y(\mathbf{y}) = W_y(\mathbf{y}, t = 0). \tag{8}$$

The image obtained with this imaging procedure is shown in Figure 6d. As in the preceding case, the artifacts caused by the unknown random fluctuations in the model are reduced, producing a cleaner image of the source, comparable with the one in Figure 6c.

Multioffset interferometric imaging condition

The imaging procedure in equations 5 and 8 can be generalized for imaging prestack (multioffset) data (Figure 1b). The conventional imaging procedure for this type of data consists of two steps (Claerbout, 1985): wavefield simulation from the source location to the image coordinates $\mathbf{y}$ and wavefield reconstruction at image coordinates $\mathbf{y}$ from data recorded at receiver coordinates $\mathbf{x}$, followed by an imaging condition evaluating the match between the simulated and reconstructed wavefields.

Let $U_S(\mathbf{y}, t)$ be the source wavefield constructed from the location of the seismic source and $U_R(\mathbf{y}, t)$ be the receiver wavefield reconstructed from the receiver locations. A conventional imaging procedure produces a seismic image as the zero lag of the time crosscorrelation between the source and receiver wavefields. Mathematically, we can represent this operation as

$$R(\mathbf{y}) = \int_t dt U_S(\mathbf{y}, t) U_R(\mathbf{y}, t), \tag{9}$$

where $R(\mathbf{y})$ represents the seismic image for a particular seismic experiment at coordinates $\mathbf{y}$.

When multiple seismic experiments are processed, a complete image is obtained by summation of the images constructed for individual experiments. The actual reconstruction methods used to produce wavefields $U_S(\mathbf{y}, t)$ and $U_R(\mathbf{y}, t)$ are irrelevant here. As in the zero-offset/exploding-reflector case, we use time-domain, finite-difference solutions to the acoustic-wave equation, but any other reconstruction technique can be applied without changing the imaging approach.

When imaging in random media, the data recorded at the surface incorporate phase delays caused by the velocity variations encountered as waves propagate in the subsurface. In a typical seismic experiment, random-phase delays accumulate both on the way from the source to the reflectors, as well as on the way from the reflectors to the receivers. Therefore, the receiver wavefield reconstructed using the background velocity model is characterized by random fluctuations, similar to the ones seen for wavefields reconstructed in the zero-offset situation.

In contrast, the source wavefield is simulated in the background medium from a known source position; therefore, it is not affected by random fluctuations. However, the zero lag of the crosscorrelations between the source wavefields (without random fluctuations) and the receiver wavefield (with random fluctuations) still generates image artifacts similar to the ones encountered in the zero-offset case.

Statistically stable imaging using pseudo-WDFs can be obtained in this case, too. What we need to do is attenuate the phase errors in the reconstructed-receiver wavefield and then apply a conventional imaging condition. Therefore, a multioffset interferometric imaging condition can be formulated as

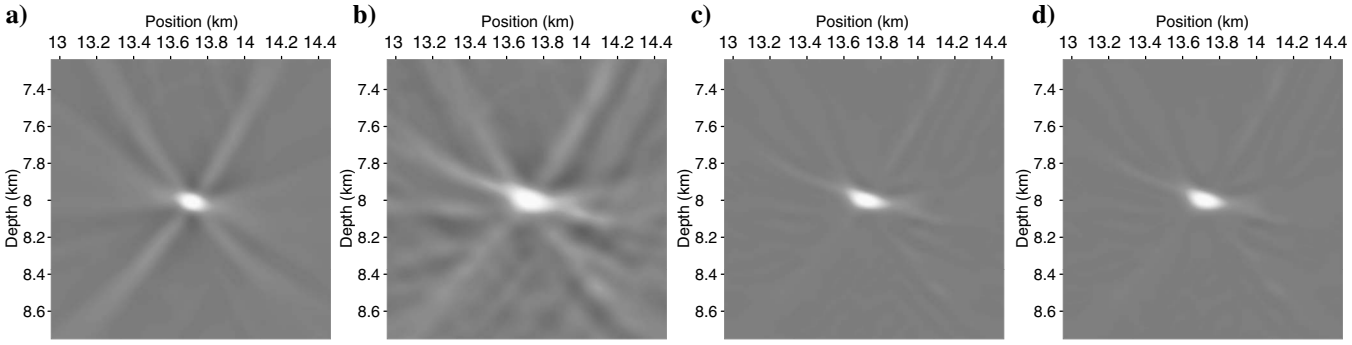


Figure 6. Images produced by the conventional imaging condition using (a) the data simulated in the background model and (b) the data simulated in the random model. Images produced from data simulated in the random model using the interferometric imaging condition with (c) parameterization as a function of data coordinates and (d) parameterization as a function of image coordinates.

$$R(\mathbf{y}) = \int_t dt U_S(\mathbf{y},t) W_R(\mathbf{y},t), \tag{10}$$

where $W_R(\mathbf{y},t)$ represents the WDF of the receiver wavefield $U_R(\mathbf{y},t)$, which can be constructed, in principle, with parameterization relative to data coordinates (equations 4–6) or relative to image coordinates (equation 5). Of course, our choice is to use image-space parameterization for computational efficiency.

DISCUSSION

The imaging procedures in equations 4, 6, and 7 and in equations 5 and 8 use wavefields reconstructed from the surface data in similar ways. Neither method uses the surface-recorded data directly, but they use wavefields reconstructed from those data as boundary conditions to numerical solutions of the acoustic-wave equation. The actual wavefield-reconstruction procedure is identical in both cases.

The techniques differ because imaging with equations 4, 6, and 7 uses independent wavefield reconstruction from receiver locations $\mathbf{x}$ to image locations $\mathbf{y}$. In practice, this requires separately solving the acoustic-wave equation, e.g., by time-domain finite differences, from all receiver locations on the surface. Such computational effort is often prohibitive. In contrast, imaging with equations 5 and 8 is similar to conventional imaging because it requires only one wavefield reconstruction using all recorded data at once, i.e. only one solution to the acoustic-wave equation, similar to conventional shot-record migration.

The techniques in equations 4, 6, and 7 and in equations 5 and 8 are similar in that they both use noise suppression using WDFs. However, the methods are parameterized differently, the former relative to data coordinates with 2D space averaging and the latter relative to image coordinates with 3D space averaging.

The imaging functionals we present are functions of space coordinates, $\mathbf{x}$ or $\mathbf{y}$ and time t. As suggested in Appendix A, WDFs can be implemented either in time or frequency, so the imaging conditions discussed in this paper potentially can be implemented in the frequency domain. However, we restrict our attention to the time-domain implementation and leave the frequency-domain implementation for future study.

Equations 4, 6, and 7 can be collected into the zero-offset imaging functional

$$R_{CINT}(\mathbf{y}) = \int_t dt \delta(t) \int_{\mathbf{x}} d\mathbf{x} \int_{|t_h| \le T} dt_h \int_{|\mathbf{x}_h| \le X} d\mathbf{x}_h \times V\left(\mathbf{x} - \frac{\mathbf{x}_h}{2}, \mathbf{y}, t - \frac{t_h}{2}\right) V\left(\mathbf{x} + \frac{\mathbf{x}_h}{2}, \mathbf{y}, t + \frac{t_h}{2}\right), \tag{11}$$

where the temporal δ function implements the zero-time imaging condition. A similar form can be written for the multioffset case. Equation 11 corresponds to the time-domain version of the coherent interferometric functional proposed by Borcea et al. (2006a, b, c). Consistent with the earlier discussion, the cost required to implement this imaging functional is often prohibitive for practical application to seismic imaging problems.

STATISTICAL STABILITY

The interferometric imaging condition described in the preceding section is used to reduce imaging artifacts by attenuating the incoherent energy corresponding to velocity errors, as illustrated in Figure 6b and d. The random model used for this example corresponds to the weak fluctuation regime, as explained in Appendix B (characteristic wavelength of similar scale with the random fluctuations in the medium and fluctuations with small magnitude).

By statistical instability, we mean that images obtained for different realizations of random models with the identical statistics are different. Figure 7a-c illustrates data modeled for different realizations of the random model in Figure 3b. The general kinematics of the data are the same, but subtle differences exist between the various data sets because of the random model variations. Migration using a conventional imaging condition leads to the images in Figure 7d-f, which also shows variations from one realization to another. In contrast, Figure 7g-i shows images obtained by the interferometric imaging condition in equations 5 and 8, which are more similar to one another because many of the artifacts have been attenuated.

In typical seismic-imaging problems, we cannot ensure that random velocity fluctuations are small (e.g., $\sigma \le 5\%$). Imaging should remain statistically stable even when velocity varies with larger magnitude. In this case, we investigate the statistical properties of the imaging functional in equations 5 and 8 using numerical experiments similar to the one used earlier. We describe the random noise present in the velocity models using seismic spatial wavelength $\lambda = 0.0762$ km; wavelet central frequency $\omega = 20$ Hz; random fluctuations parameters $r_a = 0.0762$, $r_c = 0.0762$, $\alpha = 2$; and random noise magnitude σ between 15% and 45% (see Appendix B).

The numerical experiment simulates a situation that mixes the theoretical regimes explained in Appendix C. Random model fluctuations of comparable scale with the seismic wavelength destroy the wavefronts, as suggested by the weak-fluctuation regime. The large magnitude of the random noise diffuses the wavefronts, as suggested by the diffusion-approximation regime. This combination of parameters can be regarded as a worst-case scenario theoretically.

Figure 8a-c shows data simulated in models similar to the one depicted in Figure 3b but where the random noise component is described by $\sigma = 15\%, 30\%, 45\%$, respectively. As expected, the wavefronts recorded at the surface are increasingly distorted to the point where some of the later arrivals are not even visible in the data.

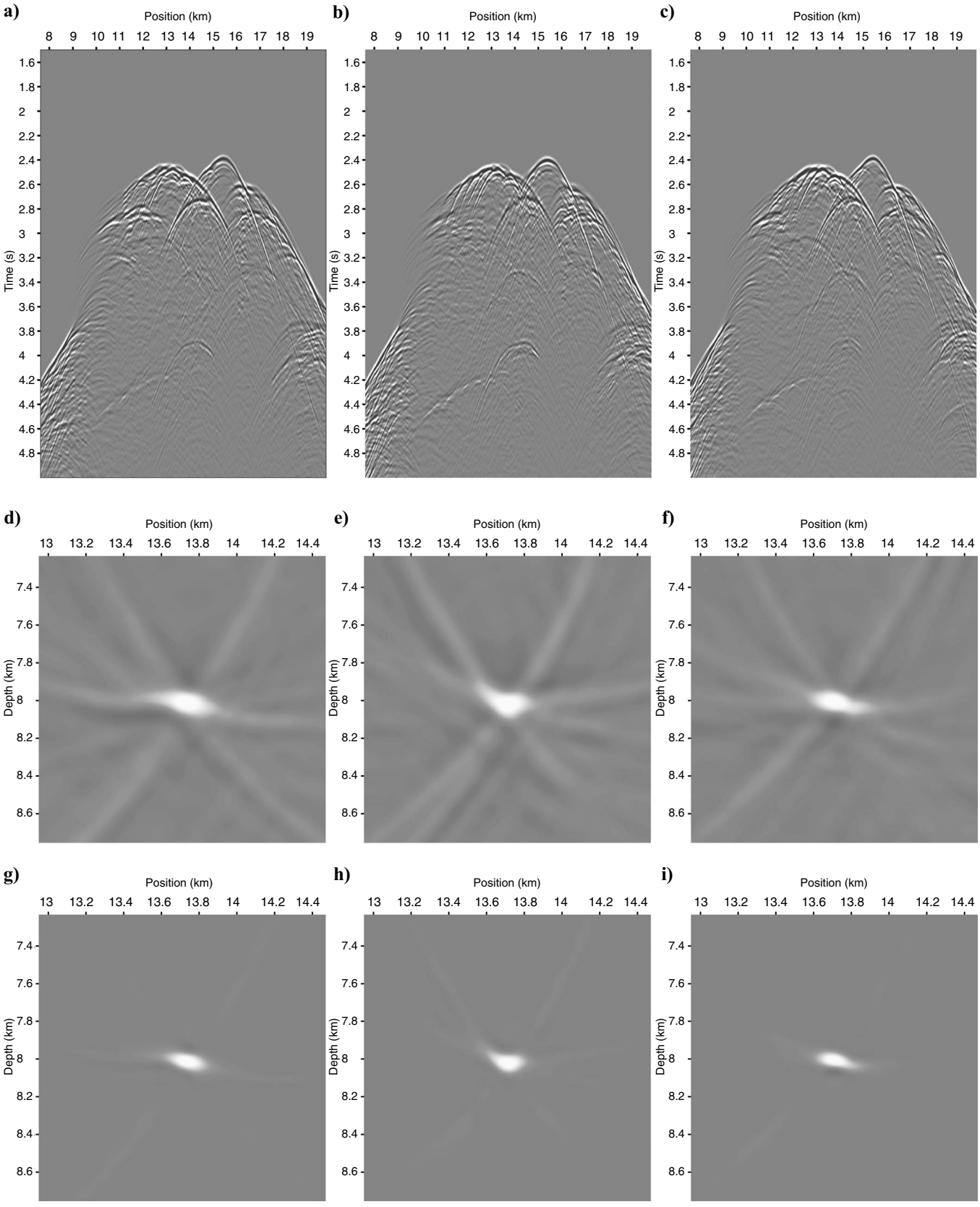


Figure 7. Statistical stability for the interferometric imaging condition in the presence of random model variations. Data modeled using velocity with random variations of magnitude $\sigma = 30\%$ for different realizations of the noise model n. Images obtained by (d)-(f) conventional imaging and (g)-(i) interferometric imaging.

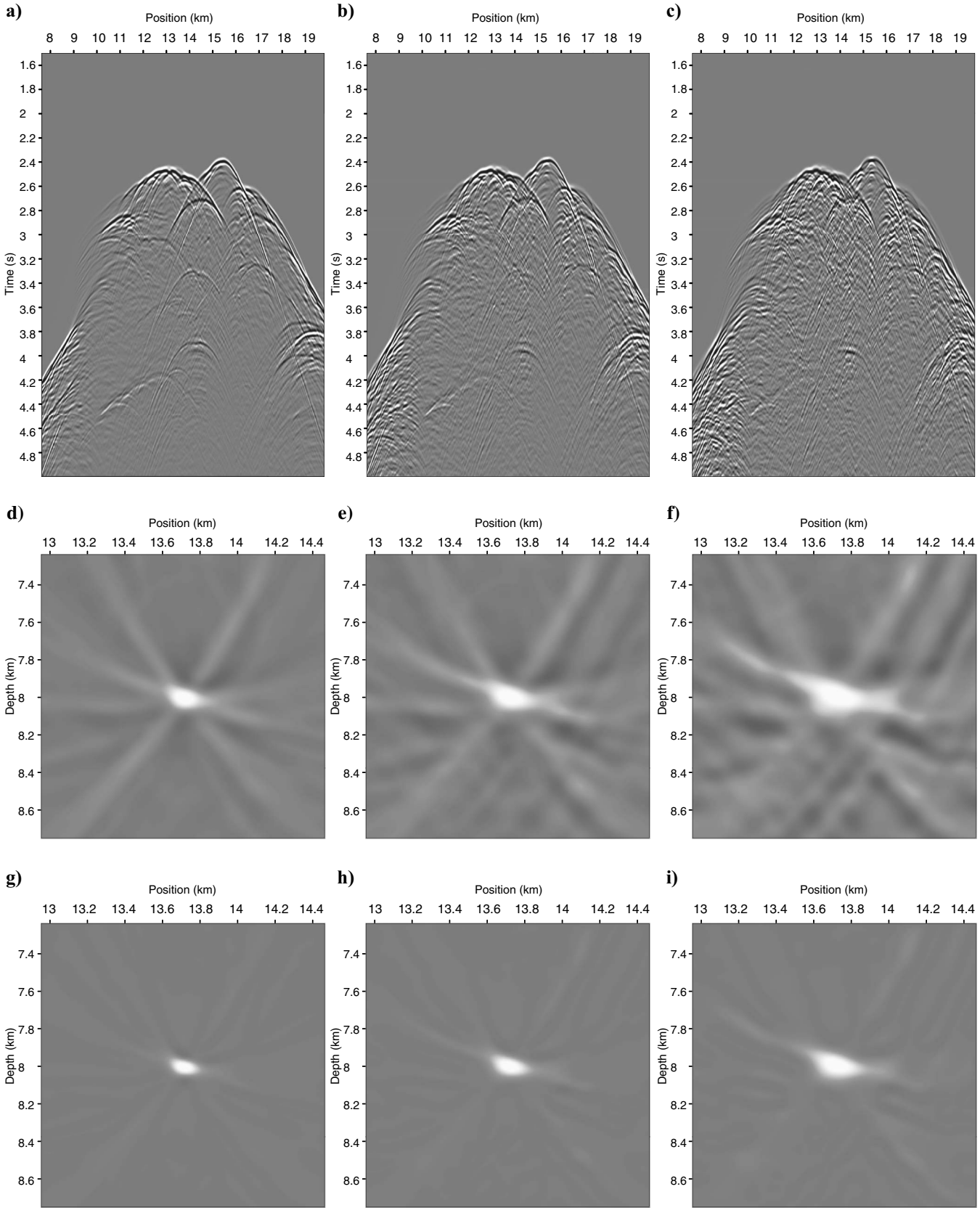


Figure 8. Interferometric imaging-condition robustness in the presence of random model variations. Data modeled using velocity with random variations of magnitudes: (a) $\sigma = 15\%$, (b) $\sigma = 30\%$, and (c) $\sigma = 45\%$. Images obtained by conventional imaging (d)-(f) and by interferometric imaging (g)-(i).

Migration using a conventional imaging condition leads to the images in Figure 8d-f. As expected, the images show stronger artifacts because of the larger defocusing caused by the unknown random fluctuations in the model. However, migration using the interferometric imaging condition leads to Figure 8g-i. Artifacts are significantly reduced, and the images are much better focused.

MULTIOFFSET IMAGING EXAMPLES

There are many potential applications for this interferometric imaging functional. One application is imaging complex stratigraphy through a medium characterized by unknown, random variations. In this situation, accurate imaging using conventional methods requires velocity models that incorporate the small-scale (random, as we view them) velocity variations. However, practical migration-velocity analysis does not produce models of this level of accuracy-but approximates them with smooth, large-scale fluctuations one order of magnitude larger than that of the typical seismic wavelength. Here, we study the impact of the unknown (random) component of the velocity model on the images and whether interferometric imaging increases the statistical stability of the image.

For all of our examples, we extrapolate wavefields using time-domain finite differences both for modeling and for migration. Thus, we simulate a reverse-time imaging procedure, although our theoretical results apply equally well to other wavefield-reconstruction techniques, e.g., downward-continuation, Kirchhoff-integral methods, etc. The parameters used in our examples, explained in Appendix B, are seismic spatial wavelength $\lambda = 0.0762$ km; wavelet central frequency $\omega = 20$ Hz; random fluctuations parameters $r_a = 0.0762$ km, $r_c = 0.0762$ m, $\alpha = 2$; and random noise magnitude $\sigma = 20\%$.

Consider the model depicted in Figure 9a and b. As in the preceding example, the left panels depict the known smooth velocity v_0, and the right panels depict the model with random variations. The imaging target is represented by the oblique lines (Figure 9b), located around $z = 8$ km, which simulates a cross section of a stratigraphic model.

We model data with a random velocity model and image using the smooth model. Figure 10a-d shows wavefield snapshots in the two models for different propagation times, one before the source wavefields interact with the target reflectors and one after this interaction. The propagating waves are affected by the random fluctuations in the model both before and after their interaction with the reflectors. Figure 10e and f shows the corresponding recorded data on the acquisition surface located at $z = \lambda$, where λ represents the wavelength of the source pulse.

Migration with a conventional imaging condition of the data simulated in the background model using the same velocity produces the image in Figure 11a. The targets are well imaged, although the image also shows artifacts caused by truncation of the data on the acquisition surface. In contrast, migration with the conventional imaging condition of the data simulated in the random model using the background velocity produces the image in Figure 11b. This image is distorted by the random variations in the model that are not accounted for in the background migration velocity. The targets are harder to discern because they overlap with many truncation and defocusing artifacts caused by the inaccurate migration velocity.

Finally, Figure 11c shows the migrated image using the interferometric imaging condition applied to the wavefields reconstructed by the background model from the data simulated in the random model. Many of the artifacts caused by the inaccurate velocity model are suppressed, and the imaging targets are more clearly visible and easier to interpret. Furthermore, the general patterns of amplitude variation along the imaged reflectors are similar between Figure 11b and c.

We note that the reflectors are not as well imaged as the ones obtained when the velocity is perfectly known. This is because the interferometric imaging condition described in this paper does not correct kinematic errors caused by inaccurate velocity. It only acts on the extrapolated wavefields to reduce wavefield incoherency and add statistical stability to the imaging process. Further extensions to the interferometric imaging condition can improve focusing and enhance the images by correcting wavefields prior to imaging. However, this topic falls outside the scope of this work.

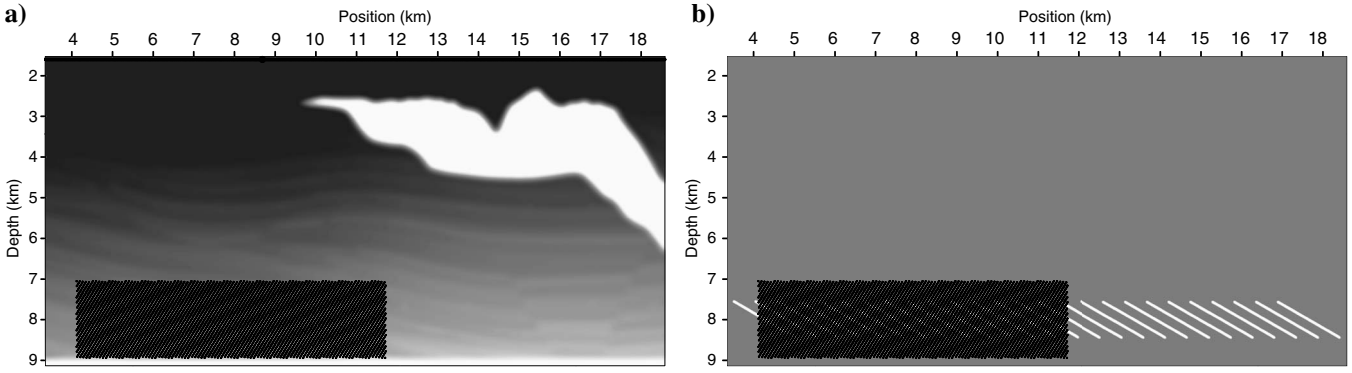


Figure 9. (a) Velocity model and (b) imaging target located around $z = 8$ km. The model consists of a smooth version of the Sigsbee2A velocity to avoid backscattering during reverse-time migration. The shaded area is imaged in Figure 11.

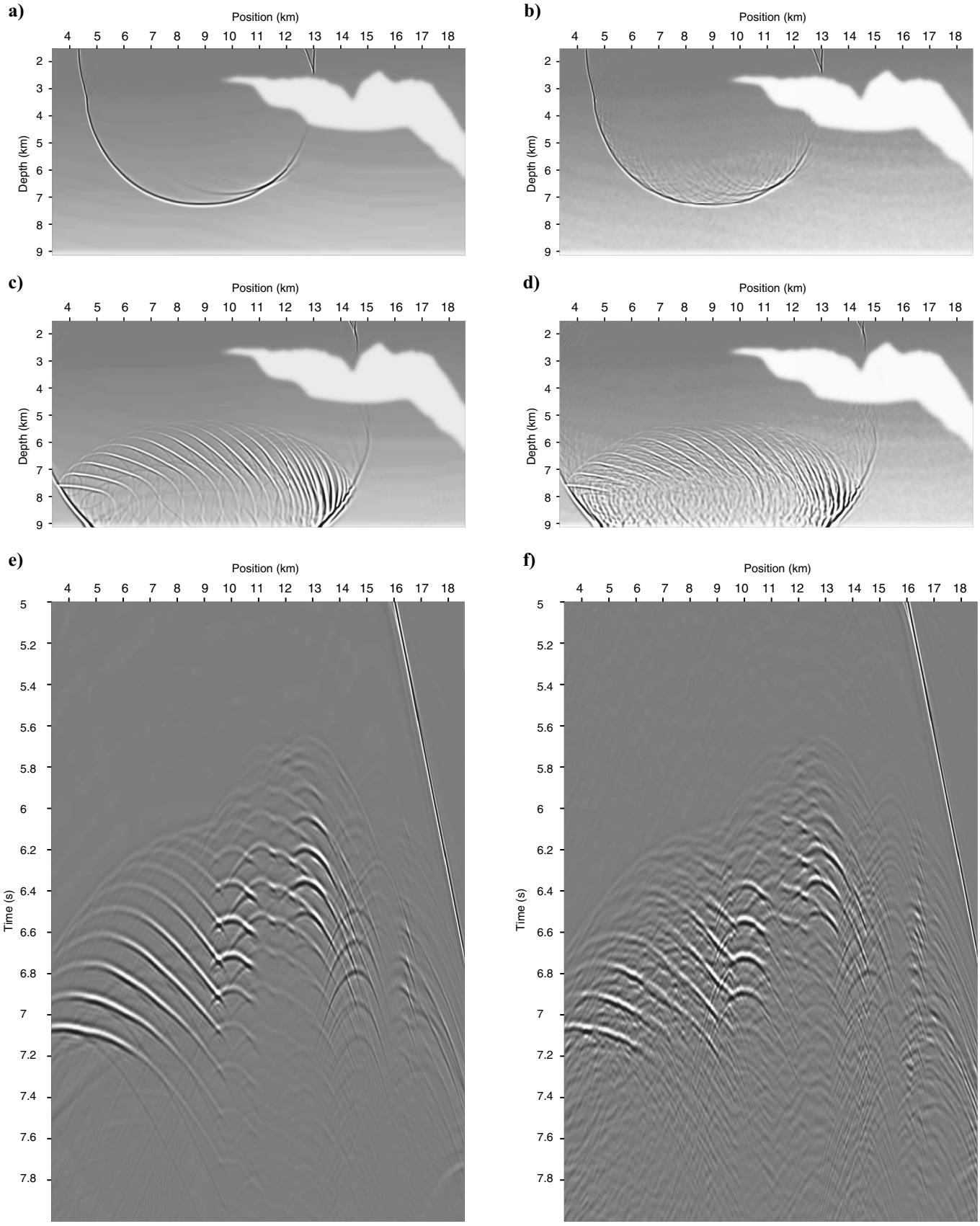


Figure 10. Seismic snapshots of acoustic wavefields simulated (a and c) in the background velocity model and (b and d) in the random velocity model. Data recorded at the surface from (e) the simulation in the background velocity model and (f) the simulation in the random velocity model.

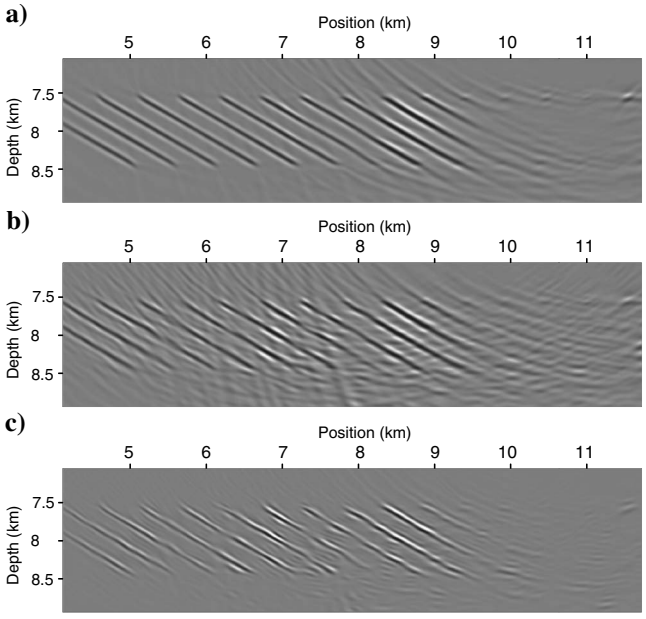


Figure 11. Images produced using the conventional imaging condition from (a) data simulated in the background model and (b) data simulated in the random model. (c) Image produced using the interferometric imaging condition from data simulated in the random model.

CONCLUSIONS

We extend the conventional seismic imaging condition based on wavefield crosscorrelations to achieve statistical stability for models with rapid, small-scale velocity variation. We assume that the random velocity variations on a scale comparable to the seismic wavelength are modeled by correlated Gaussian distributions. Our proposed interferometric imaging condition achieves statistical stability by applying conventional imaging to the WDFs of the reconstructed seismic wavefields. The interferometric imaging condition is a natural extension of the crosscorrelation imaging condition and adds minimally to the cost of migration. The main characteristic of the method is that it operates on extrapolated wavefields at image positions (thus the term interferometric imaging condition), in contrast to costlier alternative approaches using interferometry parameterized as a function of receiver coordinates.

ACKNOWLEDGMENTS

We acknowledge associate editor John Etgen for numerous comments and suggestions that significantly improved the manuscript. This work is partially supported by the sponsors of the Center for Wave Phenomena at the Colorado School of Mines.

APPENDIX A

WIGNER DISTRIBUTION FUNCTIONS

Consider the complex signal $u(t)$ that depends on time t. By definition, its WDF is (Wigner, 1932)

$$W(t,\omega) = \frac{1}{2\pi}\int u^*\left(t - \frac{t_h}{2}\right)u\left(t + \frac{t_h}{2}\right)e^{-i\omega t_h}dt_h, \tag{A-1}$$

where ω denotes temporal frequency, t_h denotes the relative time shift of the considered signal relative to a reference time t, and the asterisk denotes complex conjugation of complex signal $u(t)$.

The same WDF can be obtained in terms of the spectrum $U(\omega)$ of the signal $u(t)$:

$$W(t,\omega) = \frac{1}{2\pi}\int U^*\left(\omega - \frac{\omega_h}{2}\right)U\left(\omega + \frac{\omega_h}{2}\right)e^{-it\omega_h}d\omega_h, \tag{A-2}$$

where ω_h denotes the relative frequency shift of the considered spectrum relative to a reference frequency ω. The time integral in equation A-1 or the frequency integral in equation A-2 spans the entire domain of time and frequency, respectively. When the interval is limited to a region around the reference value, the transformation is known as pseudo-WDF.

A special subset of the transformation in equation A-1 corresponds to zero temporal frequency. For input signal $u(t)$, we obtain the output WDF $W(t)$ as

$$W(t) = \frac{1}{2\pi}\int u^*\left(t - \frac{t_h}{2}\right)u\left(t + \frac{t_h}{2}\right)dt_h. \tag{A-3}$$

The WDF transformation can be generalized to multidimensional signals of space and time. For example, for 2D real signals function of space $u(x,y)$, the zero-wavenumber pseudo-WDF can be formulated as

$$W(x,y) = \frac{1}{4\pi^2}\int_{|x_h|\le X}\int_{|y_h|\le Y} \times u\left(x - \frac{x_h}{2}, y - \frac{y_h}{2}\right)u\left(x + \frac{x_h}{2}, y + \frac{y_h}{2}\right)dx_h dy_h, \tag{A-4}$$

where x_h and y_h denote relative shift of the signal $u(x,y)$ relative to positions x and y, respectively. In this particular form, the pseudo-WDF transformation filters the input of random fluctuations, preserving in the output image the spatially coherent components in a noise-free background.

For illustration, consider the model depicted in Figure A-1a. This model consists of a smoothly varying background with 25% random fluctuations. The acoustic-seismic wavefield corresponding to a source located in the middle of the model is depicted in Figure A-1b. This wavefield snapshot can be considered as the random image.

Applying the 2D pseudo-WDF transformation to images shown in Figure A-1b produces the image shown in Figure A-1c. We can make three observations about this image: (1) the random noise is strongly attenuated; (2) the output wavelet is different from the input wavelet, as a result of the bilinear nature of the pseudo-WDF transformations; (3) the transformation is isotropic, i.e., it operates identically in all directions. The pseudo-WDF applied to this image uses 11×11 grid points in the vertical and horizontal directions. As indicated in the body of the paper, we do not discuss here the optimal selection of the WDF window.

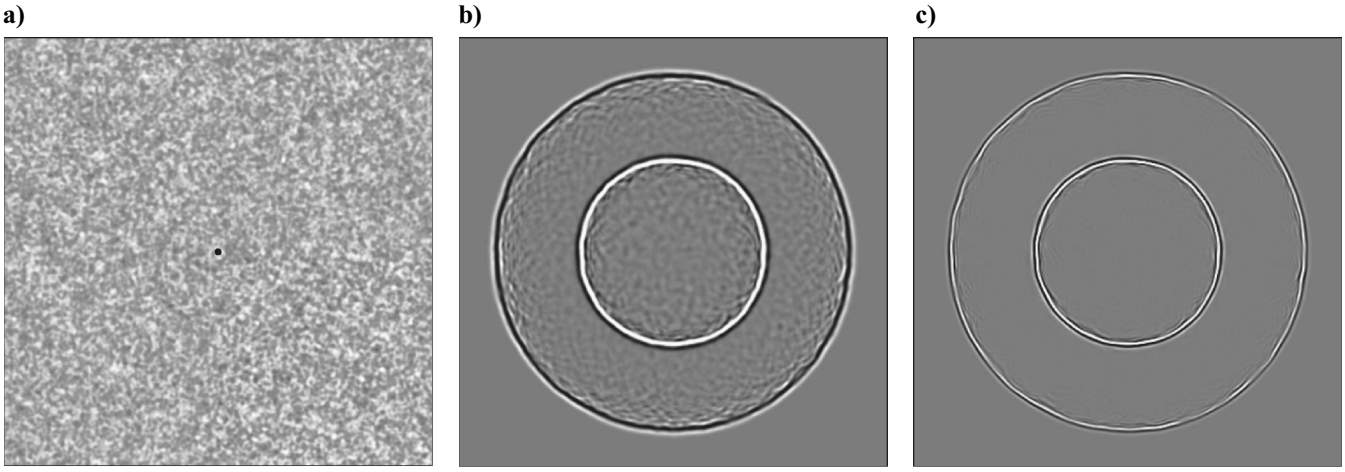


Figure A-1. (a) Random-velocity model, (b) wavefield snapshot simulated in this model by acoustic finite differences, and (c) its 2D pseudo-WDF.

Further details of WDFs and related transformations are discussed by Cohen (1995).

APPENDIX B

NOISE MODEL

Consider a medium whose behavior is completely defined by the acoustic velocity, i.e., assume that the density $\rho(x,y,z) = \rho_0$ is constant and the velocity $v(x,y,z)$ fluctuates around a homogenized value $v_0(x,y,z)$ according to the relation

$$\frac{1}{v^2(x,y,z)} = \frac{1 + \sigma m(x,y,z)}{v_0^2(x,y,z)}, \tag{B-1}$$

where m characterizes the type of random fluctuations present in the velocity model and σ denotes their strength.

Consider the covariance-orientation vectors

$$\mathbf{a} = (a_x,a_y,a_z)^T \in \mathrm{R}^3, \tag{B-2}$$

$$\mathbf{b} = (b_x,b_y,b_z)^T \in \mathrm{R}^3, \tag{B-3}$$

$$\mathbf{c} = (c_x,c_y,c_z)^T \in \mathrm{R}^3, \tag{B-4}$$

defining a coordinate system of arbitrary orientation in space. Let $r_a,r_b,r_c>0$ be the covariance-range parameters in the directions of $\mathbf{a}$, $\mathbf{b}$, and $\mathbf{c}$, respectively.

We define a covariance function

$$\mathrm{cov}(x,y,z) = \exp[-l^\alpha(x,y,z)], \tag{B-5}$$

where $\alpha \in [0,2]$ is a distribution-shape parameter and

$$l(x,y,z) = \sqrt{\left(\frac{\mathbf{a}\cdot\mathbf{r}}{r_a}\right)^2 + \left(\frac{\mathbf{b}\cdot\mathbf{r}}{r_b}\right)^2 + \left(\frac{\mathbf{c}\cdot\mathbf{r}}{r_c}\right)^2} \tag{B-6}$$

is the distance from a point at coordinates $\mathbf{r} = (x,y,z)$ to the origin in the coordinate system defined by $\{r_a\mathbf{a}, r_b\mathbf{b}, r_c\mathbf{c}\}$.

Given the independent and identically distributed (IID) Gaussian noise field $n(x,y,z)$, we obtain the random noise $m(x,y,z)$ according to the relation

$$m(x,y,z) = \mathrm{F}^{-1}[\sqrt{\widehat{\mathrm{cov}}(k_x,k_y,k_z)}\hat{n}(k_x,k_y,k_z)], \tag{B-7}$$

where k_x,k_y,k_z are wavenumbers associated with the spatial coordinates x,y,z, respectively. Here,

$$\widehat{\mathrm{cov}} = \mathrm{F}[\mathrm{cov}], \tag{B-8}$$

and

$$\hat{n} = \mathrm{F}[n] \tag{B-9}$$

are Fourier transforms of the covariance function cov, and the noise n, $\mathrm{F}[\cdot]$ denotes Fourier transform, and $\mathrm{F}^{-1}[\cdot]$ denotes inverse Fourier transform. The parameter α controls the visual pattern of the field, and $\mathbf{a},\mathbf{b},\mathbf{c},r_a,r_b,r_c$ control the size and orientation of a typical random inhomogeneity.

APPENDIX C

WAVE PROPAGATION AND SCALE REGIMES

Acoustic waves characterized by pressure $p(x,y,z,t)$ propagate according to the second-order acoustic-wave equation for constant density:

$$\frac{\partial^2 p}{\partial t^2} = v^2\nabla^2 p + F_\lambda(t), \tag{C-1}$$

where $F_\lambda(t)$ is a wavelet of characteristic wavelength λ.

Given the parameters l (size of inhomogeneities), λ (wavelength size), L (propagation distance), and σ (noise strength), we can define several propagation regimes.

The weak fluctuations regime is characterized by waves with wavelength of a size comparable to that of typical inhomogeneities propagating over a medium with small fluctuations to a distance of many wavelengths. This regime is characterized by negligible backscattering, and the randomness impacts the propagating waves through forward multipathing. The relevant length parameters are related by

$$l \sim \lambda \ll L, \tag{C-2}$$

and the noise strength is assumed small:

$$\sigma \ll 1. \tag{C-3}$$

The diffusion approximation regime is characterized by waves with wavelength much larger than that of typical inhomogeneities propagating over a medium with strong fluctuations to a distance of many wavelengths. This regime is characterized by traveling waves that are statistically stable but diffuse with time. Back propagation of such waves in a medium without random fluctuations results in loss of resolution. The relevant length parameters are related by

$$l \ll \lambda \ll L, \tag{C-4}$$

and the noise strength is not assumed small:

$$\sigma \sim 1. \tag{C-5}$$

REFERENCES

Baysal, E., D. D. Kosloff, and J. W. C. Sherwood, 1983, Reverse time migration: Geophysics, **48**, 1514–1524.

Borcea, L., G. Papanicolaou, and C. Tsogka, 2006a, Adaptive interferometric imaging in clutter and optimal illumination: Inverse Problems, **22**, 1405–1436.

———, 2006b, Coherent interferometric imaging in clutter: Geophysics, **71**, no. 4, SI165–SI175.

———, 2006c, Coherent interferometry in finely layered random media: SIAM Journal on Multiscale Modeling and Simulation, **5**, 62–83.

Claerbout, J. F., 1985, Imaging the earth's interior: Blackwell Scientific Publications, Inc.

Cohen, L., 1995, Time-frequency analysis: Theory and application: Prentice-Hall, Inc.

Fink, M., 1999, Time-reversed acoustics: Scientific American, **281**, 91–97.

Fouque, J., J. Garnier, A. Nachbin, and K. Solna, 2005, Time reversal refocusing for point source in randomly layered media: Wave Motion, **42**, 191–288.

Loewenthal, D., L. Lu, R. Roberson, and J. Sherwood, 1976, The wave equation applied to migration: Geophysical Prospecting, **24**, 380–399.

Papanicolaou, G., L. Ryzhik, and K. Solna, 2004, Statistical stability in time reversal: SIAM Journal on Applied Mathematics, **64**, 1133–1155.

Pratt, R. G., 1990, Inverse theory applied to multi-source cross-hole tomography: Part 2: Elastic wave-equation method: Geophysical Prospecting, **38**, 311–312.

Pratt, R. G., and M. H. Worthington, 1990, Inverse theory applied to multi-source cross-hole tomography: Part 1: Acoustic wave-equation method: Geophysical Prospecting, **38**, 287–310.

Sava, P., and B. Biondi, 2004a, Wave-equation migration velocity analysis — I: Theory: Geophysical Prospecting, **52**, 593–606.

———, 2004b, Wave-equation migration velocity analysis — II: Subsalt imaging examples: Geophysical Prospecting, **52**, 607–623.

Shen, P., W. Symes, S. Morton, and H. Calandra, 2005, Differential semblance velocity analysis via shot profile migration: 74th Annual International Meeting, SEG, Expanded Abstracts, 2249–2253.

Sirgue, L., and R. Pratt, 2004, Efficient waveform inversion and imaging, a strategy for selecting temporal frequencies: Geophysics, **69**, 231–248.

Tarantola, A., 1987, Inverse problem theory: Methods for data fitting and model parameter estimation: Elsevier Science Publ. Co., Inc.

Ville, J., 1948, Theorie et applications de la notion de signal analytique: Cables et Transmissions, **2A**, 61–74.

Wigner, E., 1932, On the quantum correction for thermodynamic equilibrium: Physical Review, **40**, 749–759.

Woodward, M. J., 1992, Wave-equation tomography: Geophysics, **57**, 15–26.